*Article*

# In-Situ Polymerization for Catalytic Graphitization of Boronated PAN Using Aluminum and Zirconium Containing Co-Catalysts

**Taewoo Kim [1,2], Byoung-Suhk Kim [1] , Tae Hoon Ko [1,2],* and Hak Yong Kim [1,2],***

1 Department of Nano Convergence Engineering, Jeonbuk National University, Jeonju 561756, Republic of Korea; tmdskd789@naver.com (T.K.); kbsuhk@jbnu.ac.kr (B.-S.K.)
2 Department of Organic Materials and Textile Engineering, Jeonbuk National University, Jeonju 561756, Republic of Korea
* Correspondence: kth1745@jbnu.ac.kr (T.H.K.); khy@jbnu.ac.kr (H.Y.K.); Tel.: +82-632732351 (T.H.K. & H.Y.K.)

**Abstract:** In-situ polymerization is an effective method for integrating co-catalysts homogeneously into the polymer matrix. Polyacrylonitrile (PAN)-derived highly graphitized carbon is a state-of-the-art material with diverse applications, including materials for energy storage devices, electrocatalysis, sensing, adsorption, and making structural composites of various technologies. Such highly graphitized materials can be effectively obtained through in-situ polymerization. The addition of external catalysts during in-situ polymerization not only enhances the polymerization rate but also facilitates the degree of graphitization and quality of graphitic carbon upon graphitization at moderate temperatures. In this study, we apply an in-situ polymerization technique to integrate aluminum triflate $(Al(OTf)_3)$ and zirconocene dichloride $(C_5H_5)_2ZrCl_2$ co-catalyst into a boronated polyacrylonitrile (B-PAN) matrix. The in-situ polymerization ensures the uniform distribution of the co-catalyst without aggregation, facilitating the formation of a well-ordered graphitic structure at a moderated temperature. Boronated polyacrylonitrile (B-PAN) solutions, with and without co-catalyst $(Al(OTf)_3, (C_5H_5)_2ZrCl_2$ or both) were prepared through polymerization process, dried in an oven, and then subjected to graphitization at 1250 °C with a heating rate of 1 °C min$^{-1}$ for 1 h under an $N_2$ atmosphere. The resulting graphitic carbon was characterized to determine the impact of co-catalyst on the degree of graphitization. This study provides valuable insights into synthesizing high-quality graphitic carbon materials, offering promising pathways for their scalable production through the strategic use of in-situ polymerization and co-catalysis. These materials have potential applications in various fields, including environmental technologies, energy storage, and conversion, offering a pathway to design facile and economical graphitic carbon materials.

**Keywords:** in-situ polymerization; Boronated polyacrylonitrile solution (B-PAN); co-catalyst; low temperature graphitization; graphitic carbon (GC)

## 1. Introduction

Carbon has been central to human technological development throughout history, particularly when the smelting processes revealed that metals could be extracted from ores by smelting process with charcoal. Today, carbon remains essential in various fields, including energy storage and environmental sectors, such as batteries, fuel cells, and supercapacitors, as well as pigment elastomers fillers and separation or purification technologies [1–4]. The significance of carbon materials is highlighted by the classification of graphite as a critical material due to its crucial role in refractory applications and other technologies [5]. Graphitic carbons are composed of sp$^2$ hybridized carbon atoms organized into multilayers,

with each layer consisting of a closely packed hexagonal array of carbon atoms [6]. This arrangement of carbon atoms is highly symmetric and periodic, and it can be quantitatively analyzed using diffraction techniques like X-ray diffraction (XRD) or electron diffraction, providing insights into interlayer spacing and crystallinity. Many governments now acknowledge the necessity for future carbon materials to be sustainable, addressing both environmental concerns and ensuring economic security.

Nanostructured graphitic carbons have garnered growing interest due to their exceptional properties, including high chemical stability, large accessible surface areas, and impressive thermal and electronic conductivity [7]. Various methods have been developed to create complex graphitic nanostructures, including chemical vapor deposition, arc discharge, and laser ablation, commonly used for synthesizing carbon nanotubes [8,9]. However, many of these techniques are energy-intensive and pose challenges in scalability [10]. For example, direct heating of pristine carbon materials to high temperatures (2500–3000 °C) can increase the degree of graphitization. However, this process consumes a lot of energy, and the resulting graphitization is drastically decreased due to the carbon atom rearrangement at such high temperatures. Furthermore, this method is beneficial for creating porous carbon from non-graphitizing carbon, which is usually very difficult to convert into a graphitic structure through heating [11–13]. As a result, there has been a global initiative to discover more cost-effective, scalable, and sustainable approaches for producing nanostructured graphitic carbons. Catalytic graphitization is a process that involves the transformation of amorphous carbon to graphitic carbon through heat treatment in the presence of specific metals or minerals [14]. This transformation typically occurs at low temperatures (<1000 °C) compared to traditional graphitization methods, which convert non-graphitic carbon into graphite carbon, making it cost-effective and easy to process [15–19]. Among the various synthetic polymers, polyacrylonitrile (PAN) has been extensively studied because it can be easily processed into desired forms (e.g., fibers, films, or gels), facilitating the fabrication of high-quality graphitic materials. PAN yields a higher proportion of carbon upon pyrolysis or carbonization, enhancing resource utilization and cost-effectiveness [20]. Its versatility also allows for the easy incorporation of metal additives or co-catalysts, which can improve the graphitization process [21]. Various methods, including in-situ polymerization, impregnation method, mechanical mixing, co-precipitation, etc., are employed to incorporate metal catalysts or co-catalysts into the polymer matrix [22–24]. Notably, in-situ polymerization is an innovative technique that facilitates the simultaneous PAN polymerization and the incorporation of metal salts or co-catalysts [25,26]. Introducing catalysts, co-catalysts, or additives during the polymerization process allows uniform integration within the polymer matrix, minimizing agglomeration. This facilitates graphitization during subsequent thermal treatment, accelerating the conversion of polymeric materials into graphitic carbon at lower temperatures and enhancing the quality of the resulting structure [27].

Inspired by the above considerations, we performed in-situ polymerization to integrate co-catalyst in boronated PAN polymer matric for producing highly graphitized carbon. Specifically, we incorporated aluminum and zirconium-based co-catalysts (aluminum triflate and zirconocene dichloride) in boronated-polyacrylonitrile solution (B-PANs) by in-situ polymerization, resulting in a homogenous mixture solution [28]. The prepared solutions were dried in an oven and subsequently graphitized in a tube furnace at nitrogen temperature. The impact of the different co-catalysts on the graphitization of the B-PAN solution was then thoroughly characterized. This study provides a pathway for uniform integration of co-catalysts and valuable insights into how co-catalysts influence both polymerization and graphitization in B-PAN solutions, elucidating the key factors affecting the structural and compositional properties of the resulting graphitic carbon. The novelty of

this work is the integration of co-catalysts (AL and Zr) by in-situ polymerization and the study of their effect on graphitization.

## 2. Experimental

*2.1. Chemical and Materials*

The details of requisite materials and characterizations are described in the Supporting Information File (ESI).

*2.2. In-Situ Polymerization of Boronated-Polyacrylonitrile-Co-Catalyst (B-PAN$_M$; M = Co-Catalyst Containing Al and Zr)*

The boronated-PAN polymer solution was prepared by dissolving acrylonitrile (104.2 g), itaconic acid (0.91 g), 1-dodecanethiol 1.35 g, 2,2′-azobisisobutyronitrile (0.49 g), and dibutyl vinylboronate (1.24 g) in 350 mL of DMSO in a three-necked glass vessel; this solution was designated as Solution-A. Polymerization was initiated, and after 30 min, 35 mL of a DMSO solution containing aluminum triflate (Al(OTf)$_3$, 1.5 g) co-catalyst was added to Solution-A during the polymerization process. The in-situ polymerization continued for 13 h, and the resulting viscous solution was designated as B-PAN$_{Al}$. Similarly, another 35 mL of a DMSO solution containing zirconocene dichloride ((C$_5$H$_5$)$_2$ZrCl$_2$, 1.5 g) co-catalyst was added to a separate Solution-A mixture. The in-situ polymerization was also conducted for 13 h at 64 °C, and the resulting viscous solution was designated as B-PAN$_{Zr}$.

For comparative analysis, 1.5 g in 35 mL of a DMSO solution containing both Al(OTf)$_3$ and (C$_5$H$_5$)$_2$ZrCl$_2$) in a 1:1 ratio was added to solution-A, and polymerization was carried out, yielding a polymer solution designated as B-PAN$_{Al+Zr}$. As a control, a pure PAN polymer solution was prepared by dissolving acrylonitrile, itaconic acid, 1-dodecanethiol, 2,2′-azobisisobutyronitrile, and itaconic acid (without dibutyl vinylboronate) in 350 mL of DMSO in a three-necked glass vessel for comparative study.

*2.3. Graphitization of the Boronated-Polyacrylonitrile-Co-Catalyst (B-PAN$_M$-GC; M = Co-Catalyst Containing Al and Zr)*

The obtained viscous polymer solutions (B-PAN$_{Al}$, B-PAN$_{Zr}$, and B-PAN$_{Al+Zr}$) were cast on a plane surface and placed in an oven to form sold materials. The resulting solid samples were then stabilized at 250 °C and subsequently subjected to carbonization in a tube furnace under N$_2$ atmosphere at 1250 °C with a heating rate of 1 °C min$^{-1}$ for 1 h. The materials obtained after graphitization were designated as B-PAN$_{Al}$-GC, B-PAN$_{Zr}$-GC, and B-PAN$_{Al+Zr}$-GC, corresponding to the respective metal-containing compound used in the polymerization process.

## 3. Results and Discussion

*Synthesis and Structural Analysis*

The Al and Zr containing co-catalyst grafted boronated-PAN polymer solution and graphitized carbon materials were synthesized, as illustrated in Figure 1, through an in-situ polymerization and carbonization process. A pure PAN polymer solution was prepared via standard polymerization without the addition of any chemical reagents and co-catalysts. The boronated-PAN polymers were synthesized by adding a divinyl boronated compound during the PAN polymerization for a comparative study of graphitization. Similarly, co-catalyst grafted boronated-PAN polymers were prepared by adding both divinyl boronated compound and co-catalyst during PAN polymerization, a process referred to as in-situ polymerization). Figure S1a–c demonstrates the photographic images of solidified B-PAN$_{Al}$, solidified B-PAN$_{Zr}$, and solidified B-PAN$_{Al+Zr}$ polymer before graphitization. The surface structure and morphology of the synthesized samples were analyzed using FE-SEM.

Figure S2 shows the Fe-SEM image of PAN before graphitization, highlighting an irregular structure, and its elemental mapping confirms the presence of key elements, including carbon C, N, O, and S in polymerized solution. In Figure S3, the FE-SEM of boronated PAN (B-PAN) before graphitization displays a distinct layered structure, with elemental mapping indicating the distribution of essential elements such as B, C, N, O, and S. The FE-SEM images (Figure S4a–c) reveal distinct morphology, while the corresponding elemental mapping (Figure S4d–$d_5$) provides insights into the material's compositional uniformity and elemental distribution of Al, B, C, N, O, and S across the sample before graphitization. Similarly, the FE-SEM images (Figure S5a–c) reveal distinct morphology, with elemental mapping (Figure S5d–$d_5$) supporting the well distribution of Zr, B, C, N, O, and S during in-situ polymerization. Additionally, Figure S6 depicts the FE-SEM of boronated PAN (B-PAN) along with Al and Zr containing Co-catalyst before graphitization, displaying a distinct layered structure The elemental mapping indicating the distribution of essential elements such as Al, Zr, B, C, N, O, and S across the sample, suggesting the effective incorporation of aluminum and zirconium into the carbon matrix through the in-situ polymerization process. This uniform integration of Al and Zr atoms catalyzes the graphitization of the B-PAN, promoting the formation of a well-ordered carbon structure at lower temperatures. Overall, the results indicate that the in-situ polymerization with Al, and Zr co-catalysts has effectively facilitated the formation of a high-quality graphitic structure with uniform elemental composition, which is advantageous for applications in various fields. The FE-SEM images and elemental mapping of PAN-GC after graphitization (Figure S7) reveal an irregular structure with essential elements in the carbon matrix. Similarly, The FE-SEM images of B-PAN-GC (Figure S8) display the distinct morphology after graphitization, and its elemental mapping confirms the presence of essential elements in the carbon matrix even after the graphitization process.
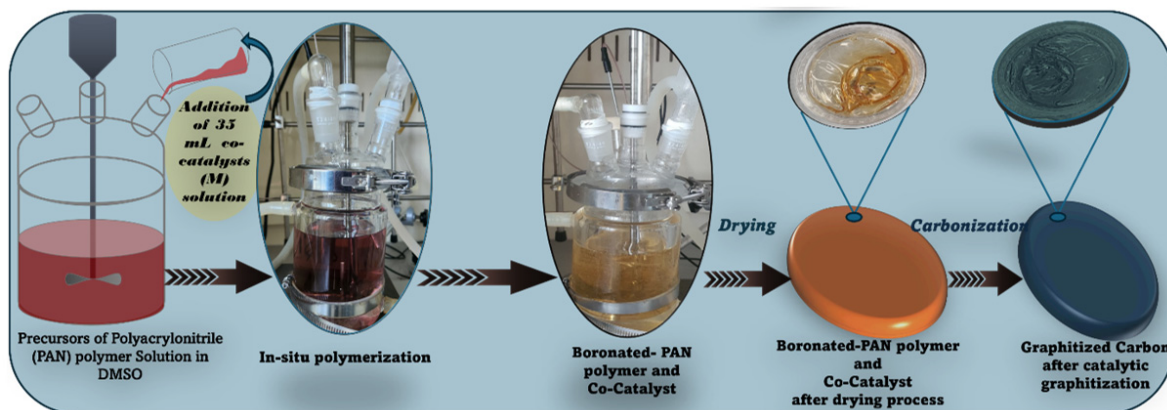


**Figure 1.** Schematic representation of the in-situ polymerization and synthesis of PANs-based graphitic carbon.

The FE-SEM images of aluminum-integrated boronated PAN after carbonization (B-PAN$_{Al}$-GC) are presented in Figure 2a,b, highlighting significant morphological changes after carbonization. These alterations are attributed to the interaction between the homogenously integrated Al metal and B-PAN-based carbon matrix during the carbonization, which promotes the development of a unique structure. The nanoparticles on the surface and roughness after graphitization The elemental mapping analysis presented in Figure 2c–$c_5$ provides a detailed view of elemental composition, confirming the effective and uniform integration of Al metal within the polymer matrix through in-situ polymerization.
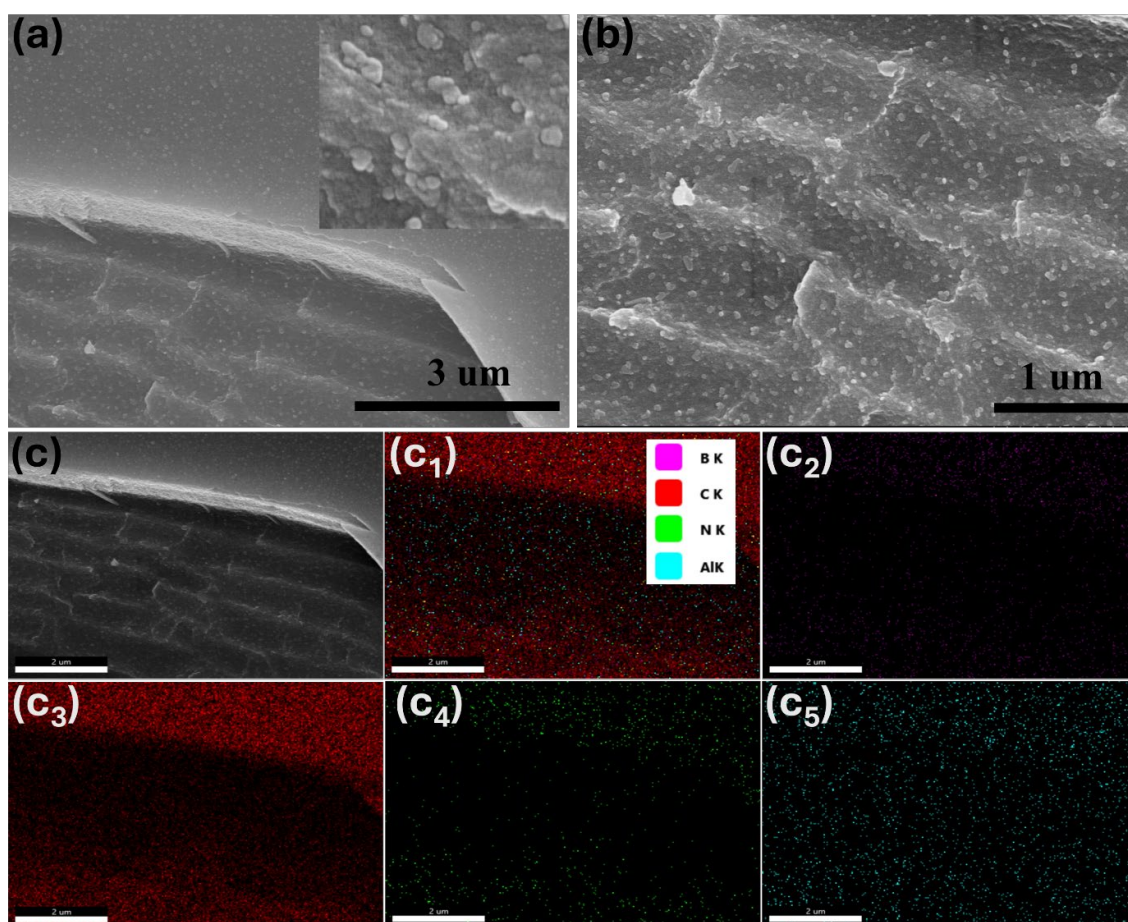
**Figure 2.** Morphological characterizations: (**a**–**c**) FE-SEM images of B-PAN$_{Al}$-GC, and (**c**–**c$_5$**) its elemental mapping after graphitization.

Similarly, FE-SEM images of zirconium-integrated boronated PAN after carbonization (B-PAN$_{Zr}$-GC) are presented in Figure 3a,b, revealing significant surface morphological changes after carbonization. These alterations result from the interaction between the homogenously integrated Zr metal and B-PAN-based carbon during the carbonization process, leading to more pronounced morphological changes and increased granulated structure on graphitized carbon materials. The elemental mapping analysis presented in Figure 3c–c$_5$ provides detailed insights into integrated elements in synthesized polymer materials, even the carbonization process of the synthesized materials, confirming that the Zr metal is effectively and uniformly integrated into the polymer matrix by in-situ polymerization. Additionally, the FE-SEM images of graphitized carbon materials in which Al and Zr contain co-catalysts during polymerization on B-PAN are shown in Figure 4a,b. The irregular surface morphology changed after graphitization due to the simultaneous interaction of both co-catalysts with B-PAN. The elemental mapping (c, c$_1$, c$_2$, c$_3$, c$_4$, c$_5$, and c$_6$) reveals the uniform distribution of both co-catalysts into the boronated carbon matrix during the polymerization, suggesting a positive effect on the graphitization of B-PANs-based carbon materials. This uniform distribution of metal-containing co-catalysts, along with the presence of boron, carbon, and nitrogen through in-situ polymerization, demonstrates the successful synthesis of a well-defined carbonized structure with potential applications in advanced materials.
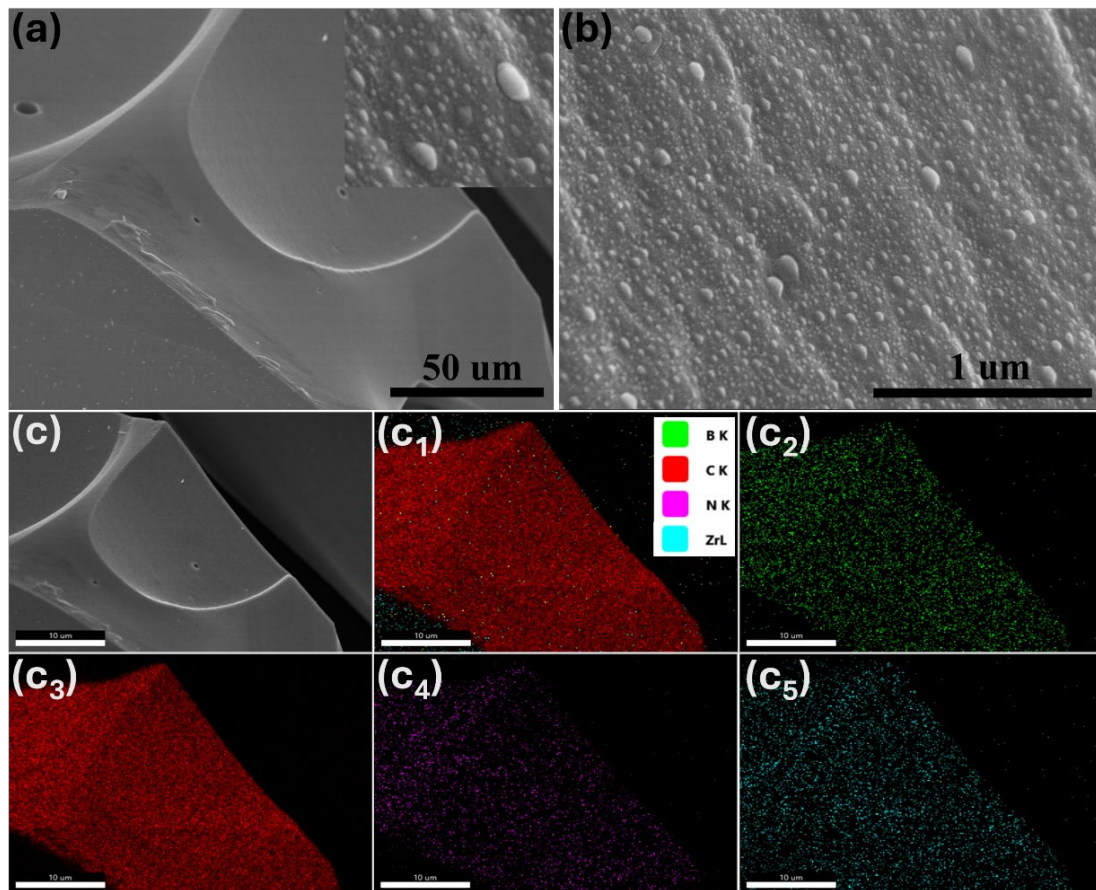
**Figure 3.** Morphological characterizations: (**a–c**) FE-SEM images of B-PAN$_{Zr}$-GC and (**c–c$_5$**) its elemental mapping after graphitization.
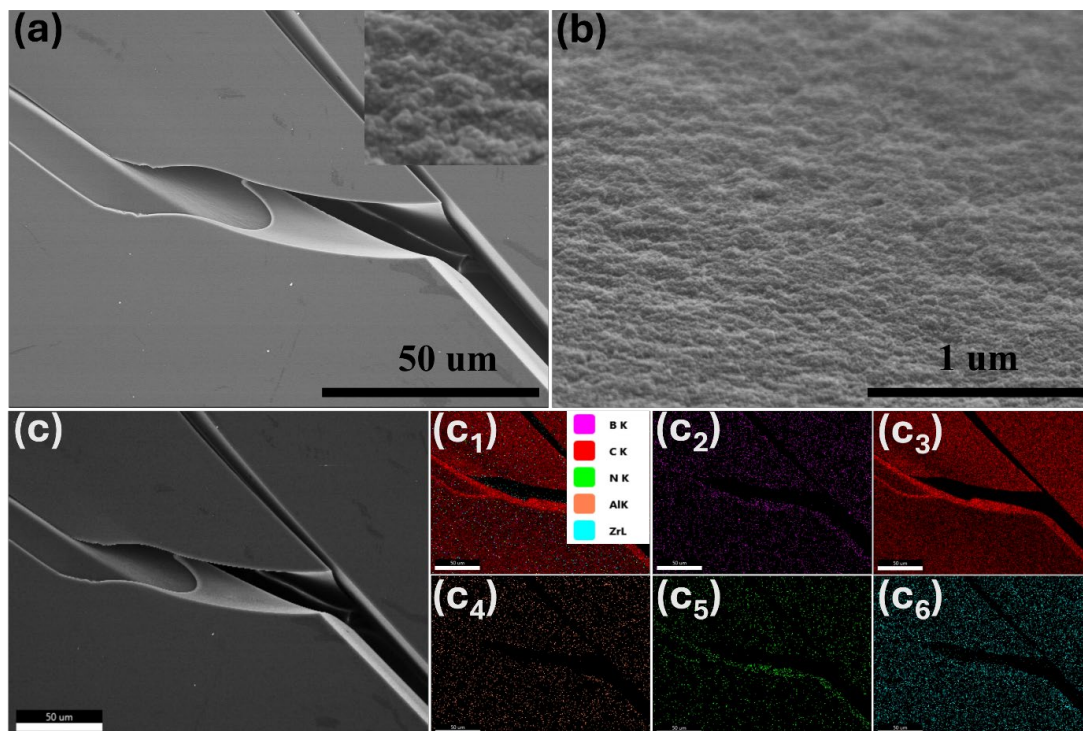


**Figure 4.** Morphological characterizations: (**a–c**) FE-SEM images of B-PAN$_{Al+Zr}$-GC and (**c–c$_6$**) its elemental mapping after graphitization.

X-ray diffraction (XRD) was employed to analyze the changes in bulk crystallinity structural order of all prepared materials, such as B-PAN$_{Al}$-GC, B-PAN$_{Zr}$-GC, B-PAN$_{Al+Zr}$-GC, B-PAN-GC as well as pure PANs after carbonization, as presented in Figure 5a. The XRD patterns of these materials reveal characteristic peaks around ~25° and 43°, which correspond to the (002) and (100) planes of graphitic carbon derived from PAN polymer [29,30]. The intensity of these peaks reflects the crystallinity and structural order within the carbon matrix [20]. The broad and low-intensity peak of pristine PAN-GC exhibits the lowest graphitization than other prepared materials. The slight increases in intensity peaks of B-PAN relative to pristine PAN-GC indicate the positive effect of boron from dibutyl vinyl boronate. The intense XRD peaks at ~25° and 43° in the presence of a co-catalyst (such as Al, Zr- containing compound) display the enhanced degree of graphitization, with sharper and more intense (002) and (100) peaks, reflecting enhanced structural order due to the catalytic effects of Al and Zr, respectively. Interestingly, the graphitized carbon containing both co-catalysts, B-PAN$_{Al+Zr}$-GC, shows improved graphitization compared to B-PAN$_{Al}$-GC and B-PAN$_{Zr}$-GC, suggesting that the combined catalytic effect of Al and Zr enhances the structural ordering required for graphitization. These findings highlight the role of the catalytic effect in enhancing graphitization and the complex interactions between dopants in influencing the structural evolution of PAN-based materials.
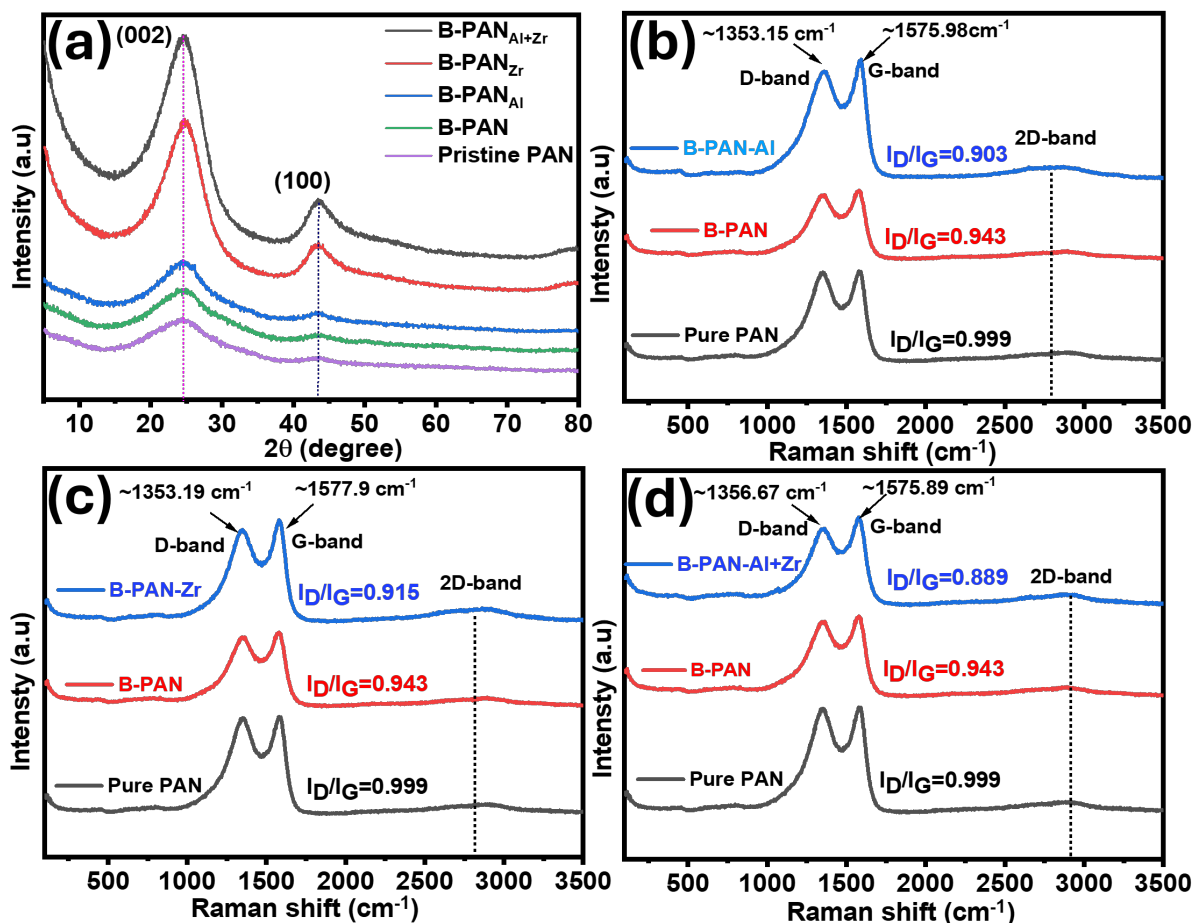


**Figure 5.** XRD analysis of (**a**) all prepared samples after graphitization, XRD analysis of (**b**) B-PAN$_{Al}$-GC, B-PAN-GC, and B-PAN-GC, (**c**) B-PAN$_{Zr}$-GC, B-PAN-GC, and B-PAN-GC, (**d**) B-PAN $_{Al+Zr}$-GC, B-PAN-GC, and B-PAN-GC after carbonization for comparative study.

Furthermore, Raman spectroscopy is a crucial technique for studying the structural and bonding characteristics of carbon-based materials, providing insight into their degree of graphitization and defect density. The Raman spectrum of carbon-based materials pri-

marily exhibits three fundamental bands: the D-band (around 1350 cm$^{-1}$), G-band (around 1580 cm$^{-1}$), and 2D-band (around 2700 cm$^{-1}$). The D-band is associated with structural defects and a disorder band within the carbon lattice, while the carbon G-band arises from the $E_{2g}$ phonon at the Brillouin zone center and represents the in-plane vibrations of sp$^2$-hybridized carbon atoms. This band signifies the crystallinity and quality of graphitic materials. A higher intensity of the D-band indicates more defects [31], whereas a higher intensity of the G-band indicates more graphitic and vice versa. Additionally, the 2D band, or G′ band, reveals the number and stacking order of graphene layers and helps quantify the disorder, crystallinity, and structural properties of carbon nanomaterials [32]. The Raman analysis results and their images are shown in Figure 6 and Figure S9, complement the XRD and FE-SEM findings by providing further insights into the structural characteristics of the synthesized graphitized materials: B-PAN, B-PAN$_{Al}$-GC, B-PAN$_{Zr}$-GC, and B-PAN$_{Al+Zr}$-GC. In the Raman spectra, all samples exhibit two main peaks: the D-band (~1350 cm$^{-1}$), associated with disordered carbon and structural defects, and the G-band (~1580 cm$^{-1}$), which corresponds to sp$^2$-hybridized carbon atoms in graphitic domains. The observed single and broad 2D-band (~2700 cm$^{-1}$) is associated with bi-layer or multilayer graphene and defects in the carbon structure after graphitization. The intensity ratio of the D-band to the G-band ($I_D/I_G$) is a crucial parameter for assessing the defect density and degree of graphitic ordering in carbon materials. Higher $I_D/I_G$ ratios indicate more disorder or defects, while lower ratios signify improved ordering. The pure B-PAN sample shows an ID/IG ratio of 0.943 in this study, suggesting a higher defect density and relatively lower graphitic order. In contrast, samples containing Al and/or Zr as co-catalysts exhibit reduced $I_D/I_G$ ratios, with B-PAN$_{Al}$-GC, B-PAN$_{Zr}$-GC, and B-PAN$_{Al+Zr}$-GC showing values of 0.903, 0.916, and 0.889, respectively. This reduction in $I_D/I_G$ values in co-catalyst-incorporated samples indicates enhanced graphitic ordering and a decrease in defects, which aligns with the XRD results, which showed an increased degree of crystallinity for these materials. The lowest $I_D/I_G$ ratio of 0.889 observed for the B-PAN$_{Al+Zr}$-GC sample implies a synergistic effect of both Al and Zr co-catalysts, leading to the most ordered graphitic structure among the samples (Table 1). This result also supports the XRD data, where the B-PAN$_{Al+Zr}$-GC sample displayed sharper and more distinct peaks, indicating greater structural order. Additionally, as presented in Table 1, comparatively prepared materials show a low ID/IG ratio, showing low-temperature graphitization. The presence of co-catalysts likely facilitates graphitization by promoting the rearrangement of carbon atoms into more ordered graphitic layers, which both the XRD and Raman analyses confirm. Overall, the Raman analysis supports the XRD findings by showing that the incorporation of Al and Zr co-catalysts in the carbon matrix reduces defect density and enhances the ordering of the graphitic structure. This improvement in structural quality is beneficial for applications requiring high conductivity and mechanical stability, as it implies a more robust and ordered carbon framework.

**Table 1.** Raman Spectroscopy Analysis of all graphitized Materials: D-band and G-band Peak Positions and $I_D/I_G$ Ratios.

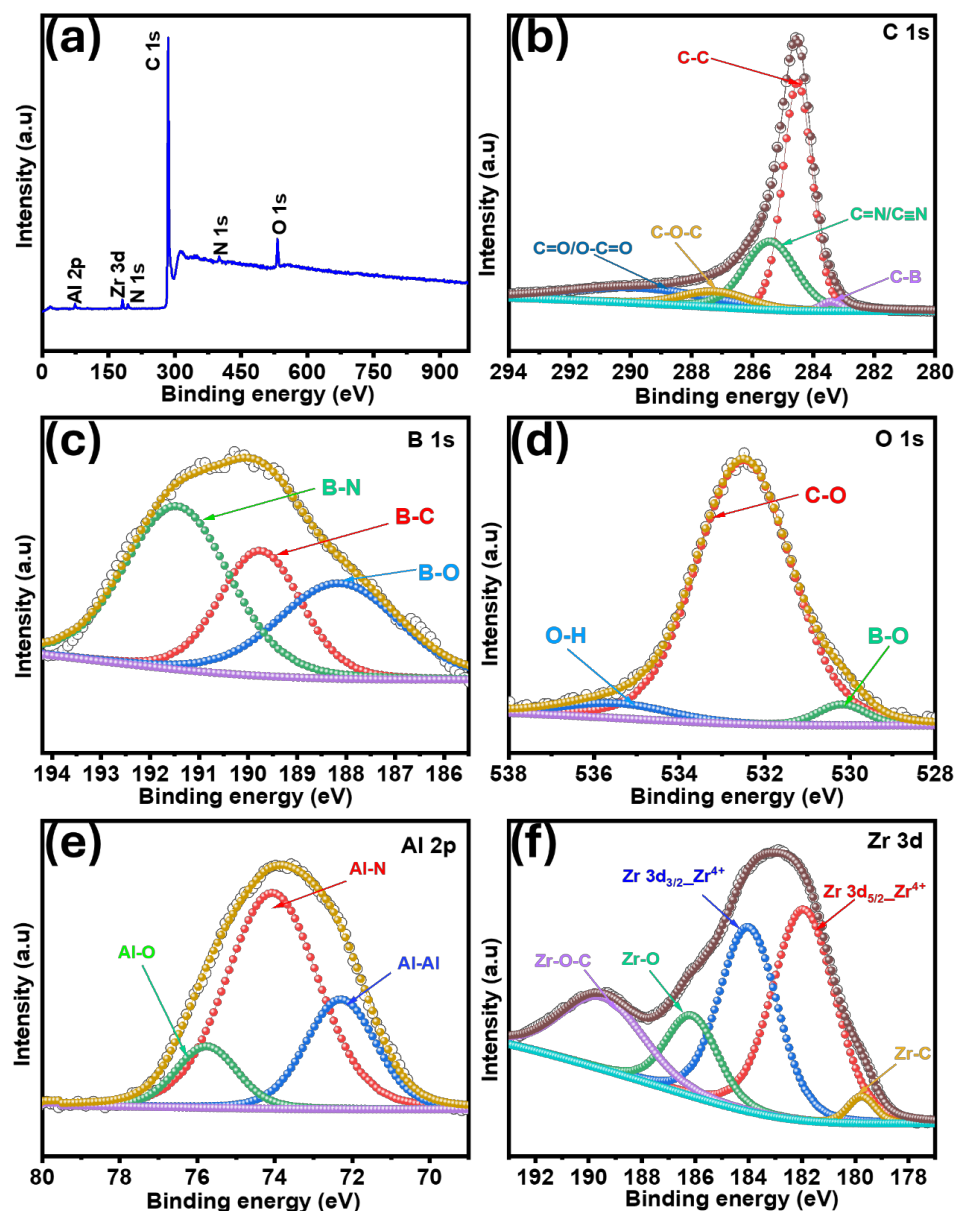| Samples | Peak Position (D-Band) (cm$^{-1}$) | Peak Position (G-Band) (cm$^{-1}$) | $I_D/I_G$ Ratio |
|---|---|---|---|
| Pure PAN-GC | 1355.46 | 1578.14 | 0.999 |
| B-PAN-GC | 41356.56 | 1575.87 | 0.943 |
| B-PAN$_{Al}$-GC | 1353.15 | 1575.98 | 0.903 |
| B-PAN$_{Zr}$-GC | 1353.19 | 1577.90 | 0.915 |
| **B-PAN$_{Al+Zr}$-GC** | **1356.67** | **1575.98** | **0.889** |

**Figure 6.** XPS analysis of B-PAN $_{Al+Zr}$-GC, (**a**) low-resolution XPS spectra, (**b**) high-resolution XPS spectra of C 1s, (**c**) high-resolution XPS spectra of B 1s, (**d**) high-resolution XPS spectra of O 1s, (**e**) high-resolution XPS spectra of Al 2p, (**f**) high-resolution XPS spectra of Zr 3d.

A survey scan XPS spectrum of B-PAN $_{Al+Zr}$-GC on the Pt plate in the range of binding energies 0–~1000 eV is shown in Figure 6a, confirms the well integration of B, C, N, Al, Zr, and O in a carbon matrix by in-situ polymerization. High-resolution XPS spectra of C 1s (Figure 6b) for the B-PAN $_{Al+Zr}$-GC show four major components including C–B (282.3–282.8 eV), C–C (~284.6 eV), C=N/C≡N (286.2–286.5 eV), and C=O/O=C–O or other oxides (288.2–288.7 eV) [33]. The dominant peak at ~284.8 eV is assigned to C–C bonds, indicating the presence of graphitic or sp$^2$ carbon structures. Peaks at higher binding energies suggest C–O, C=O, and C–N/C≡N bonds can stabilize intermediates during catalytic graphitization, aiding in the formation of graphitic layers. The B 1s spectrum (Figure 6c) shows three major peaks attributed to B–N, B–C, and B–O bonds [33,34]. The presence of B–C and B–N bonds suggests that nitrogen and boron are incorporated into the carbon matrix, providing sites that could facilitate polymer interactions. Nitrogen and boron doping are known to improve surface reactivity, which can aid in the polymerization process and enhance the compatibility between the polymer and carbon phases [35]. The

O 1s spectrum (Figure 6d) shows peaks corresponding to O–H and C=O species [36]. The O–H peak suggests absorbed moisture or hydroxyl functional groups on the surface, while the C=O peak indicates oxidized carbon structures. The Al 2p spectrum (Figure 6e) displays peaks corresponding to Al–O, Al–N, and Al–Al bonds [37,38]. The coexistence of these states implies partial oxidation of aluminum and potential incorporation in mixed-metal oxides. Similarly, The Zr 3d spectrum (Figure 6f) reveals peaks for Zr $3d_{5/2}$ and Zr $3d_{3/2}$, indicating multiple oxidation states ($Zr^{4+}$ and $Zr^{2+}$) and bonding environments, including Zr–O, Zr–C, and Zr–O–C [39,40]. These peaks suggest that zirconium exists in various oxidation states and forms both oxides and carbides. The presence of Al–Al and Zr–C/Zr–O bonds indicates that both metals are present in metallic, carbide, and oxide forms, which are active states for catalytic graphitization. Aluminum and zirconium are known to lower the activation energy for graphitization by providing sites that facilitate the reorganization of carbon atoms into a more ordered graphitic structure [41,42].

Furthermore, $^{13}$C NMR spectroscopy on all five samples was performed (Figure 7a–e), and their tacticity % is calculated and presented in Table 2. To determine the tacticity percentages, specifically isotactic (mm), atactic (mr), and syndiotactic (rr), we measured the relative intensities of methine carbon (CH) signals between 26.5 and 28 ppm in the $^{13}$C NMR spectra. Peaks near 26.8, 27.4, and 27.8 ppm are assigned to isotactic (mm), atactic (mr), and syndiotactic (rr) triads, respectively. The results revealed that all samples primarily exhibited an atactic (mr) configuration. Tacticity of the PAN, B-PAN, and B-$PAN_{Al}$ did not show significant changes. However, the boronated PAN treated with Zr shows slight changes in the tacticity % of rr, mr, and mm. Furthermore, the tacticity of B-$PAN_{Al+Zr}$ changes with the reduction in the rr%. These findings indicate that the B and Al individually do not impact PAN tacticity. But boronated PAN treated with Zr or Al + Zr alters the tacticity % of the PAN polymer. Similarly, TGA curves in Figure 7f show greater thermal stability and higher weight retention for co-catalyzed B-PAN samples, with B-$PAN_{Al+Zr}$ having the greatest retention (100.2%) due to increased graphitization efficiency. These findings emphasize the roles of Al and Zr in polymer structural modification and enhancing the graphitic properties of carbonaceous materials with improved stability.
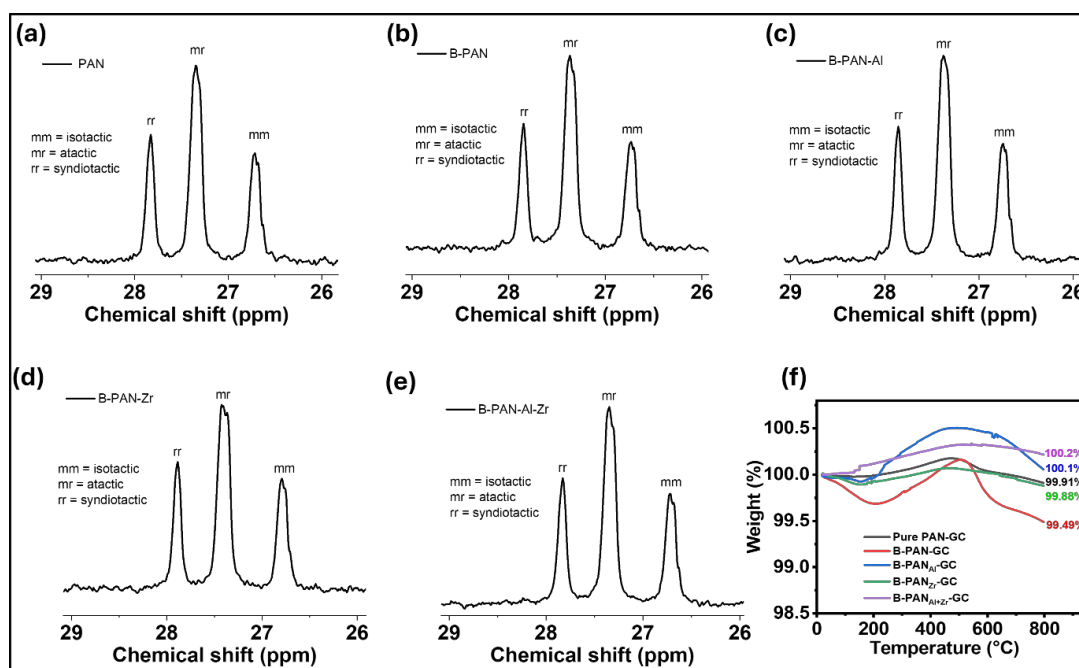


**Figure 7.** (**a–e**) $^{13}$C NMR spectra of the samples with an expanded methine carbon region, and (**f**) TGA analysis of all prepared samples.

**Table 2.** Tacticity percentage of different samples.

| S.N. | Sample Name | Tacticity (%) | | |
|---|---|---|---|---|
| | | rr | mr | mm |
| 1. | PAN | 29.28 | 45.82 | 24.9 |
| 2. | B-PAN | 29.33 | 45.69 | 24.98 |
| 3. | B-PAN$_{Al}$ | 29.29 | 45.21 | 25.5 |
| 4. | B-PAN$_{Zr}$ | 30.08 | 43.88 | 26.04 |
| 5. | B-PAN$_{Al+Zr}$ | 28.93 | 45.77 | 25.3 |

## 4. Conclusions

This work demonstrates a novel and efficient approach to synthesizing highly graphitized carbon materials by incorporating aluminum triflate (Al(OTf)$_3$) and zirconocene dichloride (($C_5H_5$)$_2$ZrCl$_2$) co-catalysts into a boronated polyacrylonitrile (B-PAN) matrix via in-situ polymerization. The in-situ polymerization process facilitated the homogeneous distribution of co-catalysts within the polymer matrix, minimizing agglomeration and enhancing the graphitization process, leading to the formation of well-ordered graphitic structures at moderated temperatures (1250 °C). Special analysis techniques such as FE-SEM, XRD, XPS, Raman analysis, NMR, and TGA analysis were used to confirm the co-catalyst-integration into B-PAN materials by in situ polymerization and to study the significant catalytic role of aluminum and zirconium in promoting graphitization. The samples containing Al and/or Zr as co-catalysts exhibit reduced $I_D/I_G$ ratios, with B-PAN$_{Al}$-GC, B-PAN$_{Zr}$-GC, and B-PAN$_{Al+Zr}$-GC showing values of 0.903, 0.916, and 0.889, respectively, which are lower than that of the sample without co-catalyst. The lowest $I_D/I_G$ ratio of 0.889 observed for the B-PAN$_{Al+Zr}$-GC sample implies a synergistic effect of both Al and Zr co-catalysts, leading to the most ordered graphitic structure among the samples. The boronated carbon materials without co-catalysts also show considerable improvement in graphitization compared to pristine PAN, highlighting the effectiveness of boron, Al, and Zr in supporting the graphitic structure. This study provides a better understanding of synthesizing high-quality graphitic carbon materials. It suggests an improved route for their production using in-situ polymerization for the integration of different co-catalysts. This technique opens an alternative way to integrate suitable co-catalysts for various applications and environmental technologies.

**Supplementary Materials:** The following supporting information can be downloaded at: https://www.mdpi.com/article/10.3390/inorganics13010016/s1, Sections S1 and S2: Experimental section with Materials and Materials characterization, Figure S1: Photographic image of: (a) solidified B-PANAl, (b) solidified B-PANZr, and (c) solidified B-PANAl + Zr polymer before graphitization. Figure S2: (a–c) FE-SEM image of PAN before graphitization, and (d–d$_5$) its elemental mapping, Figure S3: (a–c) Fe-SEM image B-PAN before graphitization, and (d–d$_5$) its elemental mapping, Figure S4: (a–c) Fe-SEM image B-PAN$_{Al}$ before graphitization, and (d–d$_5$) its elemental mapping, Figure S5: (a–c) Fe-SEM image B-PAN$_{Zr}$ before graphitization, and (d–d$_7$) its elemental mapping, Figure S6: (a–c) Fe-SEM image B-PAN$_{Al+Zr}$ before graphitization, and (d–d$_8$) its elemental mapping, Figure S7: (a,b) FE-SEM image of PAN-GC after graphitization, and (c–c$_4$) its elemental mapping, Figure S8: (a,b) Fe-SEM image B-PAN after graphitization, and (c–c$_4$) its elemental mapping, and Figure S9: Raman analysis image of: (a) PAN-GC, (b) B-PAN-GC, (b) B-PAN$_{Al}$-GC, (c) B-PAN$_{Zr}$-GC, (d) B-PAN$_{Al+Zr}$-GC. Table S1: A comparison table including terms of temperature, and graphitization degree in catalytic graphitization of carbon-based materials.

# References

1. Lower, L.; Dey, S.C.; Vook, T.; Nimlos, M.; Park, S.; Sagues, W.J. Catalytic graphitization of biocarbon for lithium-ion anodes: A minireview. *ChemSusChem* **2023**, *16*, e202300729. [CrossRef] [PubMed]

2. Pathak, I.; Dahal, B.; Acharya, D.; Chhetri, K.; Muthurasu, A.; Raj Rosyara, Y.; Kim, T.; Saidin, S.; Hoon Ko, T.; Yong Kim, H. Integrating V-doped CoP on Ti$_3$C$_2$T$_x$ MXene-incorporated hollow carbon nanofibers as a freestanding positrode and MOF-derived carbon nanotube negatrode for flexible supercapacitors. *Chem. Eng. J.* **2023**, *475*, 146351. [CrossRef]

3. Guo, S.; Wang, J.; Chen, F.; Sun, Y.; Liu, Y.; Wang, L.; Li, C. String of ZIF-derived hollow beaded nanocage embedded into carbon nanofiber with intensified exposed Co-Nx sites for efficient oxygen catalysis in various fuel cell devices. *Chem. Eng. J.* **2023**, *463*, 142498. [CrossRef]

4. Bhattarai, R.M.; Le, N.; Chhetri, K.; Acharya, D.; Pandiyarajan, S.M.S.; Saud, S.; Kim, S.J.; Mok, Y.S. Synergistic Performance Boosts of Dopamine-Derived Carbon Shell Over Bi-metallic Sulfide: A Promising Advancement for High-Performance Lithium-Ion Battery Anodes. *Adv. Sci.* **2024**, *11*, 2308160. [CrossRef] [PubMed]

5. Pusarapu, V.; Narayana Sarma, R.; Ochonma, P.; Gadikota, G. Sustainable co-production of porous graphitic carbon and synthesis gas from biomass resources. *npj Mater. Sustain.* **2024**, *2*, 16. [CrossRef]

6. Schuepfer, D.B.; Badaczewski, F.; Guerra-Castro, J.M.; Hofmann, D.M.; Heiliger, C.; Smarsly, B.; Klar, P.J. Assessing the structural properties of graphitic and non-graphitic carbons by Raman spectroscopy. *Carbon* **2020**, *161*, 359–372. [CrossRef]

7. Hunter, R.D.; Ramírez-Rico, J.; Schnepp, Z. Iron-catalyzed graphitization for the synthesis of nanostructured graphitic carbons. *J. Mater. Chem. A* **2022**, *10*, 4489–4516. [CrossRef]

8. Yang, P.-j.; Li, T.-h.; Li, H.; Dang, A.l.; Yuan, L. Progress in the graphitization and applications of modified resin carbons. *New Carbon Mater.* **2023**, *38*, 96–108. [CrossRef]

9. Lou, S.; Lyu, B.; Chen, J.; Qiu, L.; Ma, S.; Shen, P.; Zhang, Z.; Xie, Y.; Liang, Q.; Watanabe, K.; et al. Tunable growth of one-dimensional graphitic materials: Graphene nanoribbons, carbon nanotubes, and nanoribbon/nanotube junctions. *Sci. Rep.* **2023**, *13*, 4328. [CrossRef]

10. Destyorini, F.; Irmawati, Y.; Hardiansyah, A.; Widodo, H.; Yahya, I.N.D.; Indayaningsih, N.; Yudianti, R.; Hsu, Y.-I.; Uyama, H. Formation of nanostructured graphitic carbon from coconut waste via low-temperature catalytic graphitisation. *Eng. Sci. Technol. Int. J.* **2021**, *24*, 514–523. [CrossRef]

11. Yoon, S.B.; Chai, G.S.; Kang, S.K.; Yu, J.-S.; Gierszal, K.P.; Jaroniec, M. Graphitized Pitch-Based Carbons with Ordered Nanopores Synthesized by Using Colloidal Crystals as Templates. *J. Am. Chem. Soc.* **2005**, *127*, 4188–4189. [CrossRef]

12. Fuertes, A.B.; Alvarez, S. Graphitic mesoporous carbons synthesised through mesostructured silica templates. *Carbon* **2004**, *42*, 3049–3055. [CrossRef]

13. Franklin, R.E. Crystallite growth in graphitizing and non-graphitizing carbons. *Proc. R. Soc. A* **1951**, *209*, 196–218.

14. Cherakkara, A.; Zafar, S.; Izwan Misnon, I.; Yang, C.-C.; Jose, R. Graphite from biomass: A review on synthetic feasibility. *J. Ind. Eng. Chem.* **2024**, *in press*. [CrossRef]

15. Acharya, D.; Pathak, I.; Muthurasu, A.; Bhattarai, R.M.; Kim, T.; Ko, T.H.; Saidin, S.; Chhetri, K.; Kim, H.Y. In situ transmogrification of nanoarchitectured Fe-MOFs decorated porous carbon nanofibers into efficient positrode for asymmetric supercapacitor application. *J. Energy Storage* **2023**, *63*, 106992. [CrossRef]

16. Sevilla, M.; Fuertes, A.B. Catalytic graphitization of templated mesoporous carbons. *Carbon* **2006**, *44*, 468–474. [CrossRef]

17. Zhai, D.; Du, H.; Li, B.; Zhu, Y.; Kang, F. Porous graphitic carbons prepared by combining chemical activation with catalytic graphitization. *Carbon* **2011**, *49*, 725–729. [CrossRef]

18. Maldonado-Hódar, F.; Moreno-Castilla, C.; Rivera-Utrilla, J.; Hanzawa, Y.; Yamada, Y.J.L. Catalytic graphitization of carbon aerogels by transition metals. *Langmuir* **2000**, *16*, 4367–4373. [CrossRef]

19. Li, H.; Wu, A.; Qiu, Z.; Li, J.; Wu, Z.; Ma, Y.; Wang, J.; He, S.; Huang, H. Carbonization of Ni@SiC@C nanoparticles reinforced PAN nanofibers for adjustable impedance matching. *Chem. Eng. J.* **2023**, *476*, 146582. [CrossRef]

20. Shokrani Havigh, R.; Mahmoudi Chenari, H. A comprehensive study on the effect of carbonization temperature on the physical and chemical properties of carbon fibers. *Sci. Rep.* **2022**, *12*, 10704. [CrossRef]

21. Adegbola, T.A.; Agboola, O.; Fayomi, O.S.I. Review of polyacrylonitrile blends and application in manufacturing technology: Recycling and environmental impact. *Results Eng.* **2020**, *7*, 100144. [CrossRef]

22. Fawaz, J.; Mittal, V. Synthesis of Polymer Nanocomposites: Review of Various Techniques. In *Synthesis Techniques for Polymer Nanocomposites*; Wiley: Hoboken, NJ, USA, 2014; pp. 1–30.

23. Alsayed, A.F.M.; Aqeel Ashraf, M. Synthesis of Polymer Nanocomposite Films. In *Handbook of Polymer and Ceramic Nanotechnology*; Hussain, C.M., Thomas, S., Eds.; Springer International Publishing: Cham, Switzerland, 2021; pp. 157–176.

24. Stephen, R.; Pal, K.; Thomas, S. Polymer Matrix Based Nanocomposites: Preparation and Properties. In *Handbook of Polymer and Ceramic Nanotechnology*; Hussain, C.M., Thomas, S., Eds.; Springer International Publishing: Cham, Switzerland, 2020; pp. 1–15.

25. Nelson, G. 4—Microencapsulated colourants for technical textile application. In *Advances in the Dyeing and Finishing of Technical Textiles*; Gulrajani, M.L., Ed.; Woodhead Publishing: Cambridge, UK, 2013; pp. 78–104.

26. Liu, J.; Lin, H.; Li, H.; Zhao, D.; Liu, W.; Tao, X. In Situ Polymerization Derived from PAN-Based Porous Membrane Realizing Double-Stabilized Interface and High Ionic Conductivity for Lithium-Metal Batteries. *ACS Appl. Mater. Interfaces* **2024**, *16*, 21264–21272. [CrossRef] [PubMed]

27. Tang, X.; Dong, T.; Wang, M.; Ma, S.; Xu, S.; Wang, J.; Gao, B.; Huang, Y.; Yang, Q.; Hua, D.; et al. From waste corn straw to graphitic porous carbon: A trade-off between specific surface area and graphitization degree for efficient peroxydisulfate activation. *J. Hazard. Mater.* **2024**, *471*, 134422. [CrossRef]

28. Chen, L.; Yang, Z.; Yang, Y.; Yang, X.; Wang, G.; Zhu, L.; Zeng, Z. Effective solar-driven evaporators with urchin-like CuO particles and directional polyvinylidene fluoride scaffolds via directional dimethyl sulfoxide crystallization and non-solvent induced phase separation. *Sep. Purif. Technol.* **2024**, *345*, 127446. [CrossRef]

29. Hou, H.; Ge, J.J.; Zeng, J.; Li, Q.; Reneker, D.H.; Greiner, A.; Cheng, S.Z.D. Electrospun polyacrylonitrile nanofibers containing a high concentration of well-aligned multiwall carbon nanotubes. *Chem. Mater.* **2005**, *17*, 967–973. [CrossRef]

30. Zou, G.; Zhang, D.; Dong, C.; Li, H.; Xiong, K.; Fei, L.; Qian, Y.J. Carbon nanofibers: Synthesis, characterization, and electrochemical properties. *Carbon* **2006**, *44*, 828–832. [CrossRef]

31. Joni, I.M.; Vanitha, M.; Camellia, P.; Balasubramanian, N. Augmentation of graphite purity from mineral resources and enhancing % graphitization using microwave irradiation: XRD and Raman studies. *Diam. Relat. Mater.* **2018**, *88*, 129–136. [CrossRef]

32. Wang, J.; Tu, J.; Lei, H.; Zhu, H. The effect of graphitization degree of carbonaceous material on the electrochemical performance for aluminum-ion batteries. *RSC Adv.* **2019**, *9*, 38990–38997. [CrossRef] [PubMed]

33. Gu, S.; Chandra Mallick, B.; Hsieh, C.-T.; Gandomi, Y.A.; Zhang, R.-S. Hexagonal boron nitride nanosheets as metal-free electrochemical catalysts for oxygen reduction reactions. *Ceram. Int.* **2022**, *48*, 9506–9517. [CrossRef]

34. Dinescu, M.; Perrone, A.; Caricato, A.; Mirenghi, L.; Gerardi, C.; Ghica, C.; Frunza, L. Boron carbon nitride films deposited by sequential pulses laser deposition. *Appl. Surf. Sci.* **1998**, *127*, 692–696. [CrossRef]

35. Marhamati, F.; Ghaderi, M.; Haddadi, S.A.; Arjmand, M.; Olivier, M.-G.; Mahdavian, M. Nitrogen-doped carbon hollow sphere capsules for a novel hybrid inhibitor based on lanthanum cations and 8-hydroxyquinoline: Synthesis, characterization, and self-healing properties in epoxy coating. *Colloids Surf. A Physicochem. Eng. Asp.* **2023**, *675*, 132065. [CrossRef]

36. Teeparthi, S.R.; Awin, E.W.; Kumar, R. Dominating role of crystal structure over defect chemistry in black and white zirconia on visible light photocatalytic activity. *Sci. Rep.* **2018**, *8*, 5541. [CrossRef]

37. Gogoi, D.; Korde, R.; Chauhan, V.S.; Patra, M.K.; Roy, D.; Das, M.R.; Ghosh, N.N. $CoFe_2O_4$ Nanoparticles Grown within Porous $Al_2O_3$ and Immobilized on Graphene Nanosheets: A Hierarchical Nanocomposite for Broadband Microwave Absorption. *ACS Omega* **2022**, *7*, 28624–28635. [CrossRef] [PubMed]

38. Kądziołka-Gaweł, M.; Czaja, M.; Dulski, M.; Krzykawski, T.; Szubka, M. Impact of high temperatures on aluminoceladonite studied by Mössbauer, Raman, X-ray diffraction and X-ray photoelectron spectroscopy. *Mineral. Petrol.* **2021**, *115*, 431–444. [CrossRef]

39. Šekularac, G.; Kovač, J.; Milošev, I. Comparison of the Electrochemical Behaviour and Self-sealing of Zirconium Conversion Coatings Applied on Aluminium Alloys of series 1xxx to 7xxx. *J. Electrochem. Soc.* **2020**, *167*, 111506. [CrossRef]

40. Chavez-Esquivel, G.; García-Martínez, J.; De Los Reyes, J.; Suárez-Toriello, V.; Vera-Ramírez, M.; Huerta, L. The influence of $Al_2O_3$ content on $Al_2O_3$-$ZrO_2$ composite-textural structural and morphological studies. *Mater. Res. Express* **2019**, *6*, 105201. [CrossRef]

41.    Zhang, Z.-w.; Zhen, Q.; Zheng, F.; Lu, F.; Nan, C.-w.; Li, R.; Wang, J.-s. High-temperature diffusion behavior of ZrC in C matrix and its promotion on graphitization. *Trans. Nonferrous Met. Soc. China* **2016**, *26*, 2257–2262. [CrossRef]

42.    Goldie, S.J.; Coleman, K.S. Graphitization by Metal Particles. *ACS Omega* **2023**, *8*, 3278–3285. [CrossRef] [PubMed]